Signatures of Topological Phonons in Superisostatic Lattices

Olaf Stenull and T. C. Lubensky

Phys. Rev. Lett. **122**, 248002 — Published 17 June 2019

DOI: 10.1103/PhysRevLett.122.248002

Signatures of topological phonons in super-isostatic lattices

Olaf Stenull and T. C. Lubensky
Department of Physics and Astronomy, University of Pennsylvania, Philadelphia, PA 19104, USA
(Dated: May 2, 2019)

Soft topological surface phonons in idealized ball-and-spring lattices with coordination number $z = 2d$ in d dimensions become finite-frequency surface phonons in physically realizable super-isostatic lattices with $z > 2d$. We study these finite-frequency modes in model lattices with added next-nearest-neighbor springs or bending forces at nodes with an eye to signatures of the topological surface modes that are retained in the physical lattices. Our results apply to metamaterial lattices, prepared with modern printing techniques, that closely approach isostaticity.

Recent work [1–3] laid the foundation for a theory, akin to the topological band theory of electronic materials such as quantum Hall systems [4, 5] and topological insulators [6–12], of topological mechanics of periodic ball-and-spring isostatic lattices with average coordination number z, under periodic boundary conditions, equal to twice the spatial dimension, $2d$. This theory predicts the existence of zero-energy surface-modes at every surface wavenumber with the number of these modes on different surfaces depending on the topological properties of the bulk phonon spectrum. It has been applied to a variety of systems and phenomena [13–23] from random and jammed systems to stress concentration at topological domain walls. Our focus here is on periodic fully gapped systems in which the only bulk zero modes are those imposed by translational invariance at wavenumber $\mathbf{q} = \mathbf{0}$. Naturally occurring crystals always have an effective coordination number greater than $2d$ (because forces between sites have a range greater than the inter-site separation) or stabilizing bending forces favoring particular angles between bonds incident on a given site, and they are not candidates to exhibit topological mechanics. On the other hand, with the aid of modern printing and cutting techniques, metamaterials with $z = 2d$ consisting of vertices connected by thin nearest-neighbor (NN) elastic beams can be designed [18, 21] and constructed [24, 25] to minimize bending forces and, thereby, closely approach the isostatic limit to which the topological theory of Refs. [1–3] applies.

Here we study generalized kagome lattices (GKLs) to which weak next-nearest-neighbor (NNN) springs or bending forces [26] are added [Fig. 1], and we focus on how their surface modes evolve as the magnitudes v of these forces are increased from zero. In the presence of either such force, the originally isostatic lattices become stable elastic materials whose long-wavelength excitations are described by continuum elasticity, which predicts identical Rayleigh waves [27] on opposite surfaces of a strip [see supplementary information (SI)]. It would be natural to expect that these Rayleigh waves evolve from zero-energy surface modes of the isostatic lattice, and this is indeed the case for non-topological lattices, which have the same number of zero modes on all pairs of opposite parallel surfaces [1]. But this cannot be the case for topological lattices, which have opposite parallel surfaces with different numbers of zero modes –at the extreme no zero modes on one and an associated excess of zero modes on the opposite surface. In what follows, we discuss Rayleigh waves in weakly super-isostatic lattices in the context of topological phonons, and we detail how the dilemma posed by the topological lattices is resolved.

For the sake of generality, we consider generic non-topological ($X_{\rm nt}$) and topological ($X_{\rm t}$) GKLs that have the lowest possible plane crystallographic symmetry, p1. To study surface modes, we assume that a free surface parallel to the x-axis exists as indicated in Fig. 1 so that the network as a whole is semi-infinite with a parallel opposite surface located at infinite distance. For the standard GKL with $v = 0$, liberating these two surfaces from the constraints of periodic boundary conditions amounts to removing 2 bonds or 4 bonds and one site per surface unit cell. Both choices lead to two zero-surface-modes per surface wavenumber q distributed on the combined lower and upper surfaces, but the latter, which we consider, has smoother upper and lower surfaces as shown in Fig. 1. The topological polarization $\mathbf{R}_T$ [1] calculated from the bulk phonon spectrum is zero for $X_{\rm nt}$, and it is non-zero and pointing towards the bottom surface, $\mathbf{R}_T = -\frac{1}{2}(1, \sqrt{3})$, for $X_{\rm t}$. As a consequence, there is one zero-surface-mode per q on either surface for $X_{\rm nt}$ and two (zero) zero-surface-modes per q on the bottom (top) surface for $X_{\rm t}$.

Turning to $v > 0$, we will first review our results and then present some details about how we obtained them. Because of space constraints and for concreteness, we center our discussion on the case with NNN forces. Further details, model elastic energies etc., and results for the case with bending forces are provided in the SI. Figure 2 summarizes our major results about changes in the phonon band structure as the strength of the NNN coupling increases from zero and, in particular, how long-wavelength Rayleigh waves with the same speed develop on opposite surfaces and how the zero-energy surface states at $v = 0$ evolve with increasing v. At $v = 0.1$, both $X_{\rm nt}$ and $X_{\rm t}$ have one acoustic surface mode on each surface at each wavenumber q in the surface Brillouin zone (SBZ). At small q, the modes reduce to the elastic Rayleigh waves with dispersion $\omega_R(q) = c_R q$ on opposite

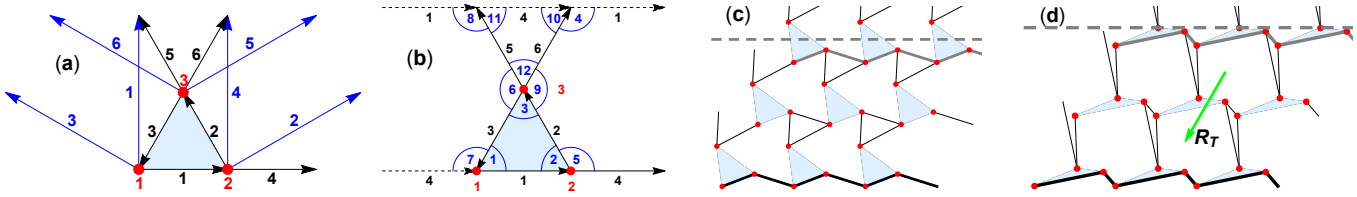

FIG. 1. (a) Unit cell of the KL with NN bonds (black) and additional NNN bonds (blue). (b) Unit cell of the KL with bending energies (blue arcs). (c) The $X_{\rm nt}$ and (d) the $X_{\rm t}$ conformation. The thick black bonds mark our bottom surface, and the thick dashed line marks a possible cut to liberate a top surface. The green arrow indicates the topological polarization R_T of $X_{\rm t}$.

surfaces with the same surface c_R, predicted by elastic theory. The situation at $v = 0.001$ is very similar to that at $v = 0.1$ for $X_{\rm nt}$ except that the acoustic surface-mode frequency $\omega_s(q)$ is smaller at every q, indicating an approach to a single zero mode at each q on each surface as $v \to 0$. Figure 2 (g) shows that $c_R \propto \sqrt{v}$ as follows from the observation that $\omega_s^2(q)$ must be linearly proportional to some combination of spring constants and be equal to zero at $v = 0$. The situation for $X_{\rm t}$ is more complex. The bottom surface has an acoustic mode that stretches across the SBZ and reduces to the expected Rayleigh wave at small q and, in addition, a low-frequency optical mode whose frequency, $\omega_{\rm opt}$ is proportional to $\sqrt{v}$ across the SBZ and that vanishes into the continuum at a critical wavenumber q_0. The top surface, on the other hand, below the lowest bulk band only has a Rayleigh wave with the same velocity as that of the bottom surface, that disappears into the bulk continuum at a wavenumber that vanishes as $v \to 0$. The two zero-frequency modes of the topological $v = 0$ lattice on the bottom surface are then the limits of the acoustic mode and the low-frequency optical mode. At $v = 0$, the bottom of the band of bulk states, $\omega_{\rm band}$, is proportional to q^2 rather than q as can be calculated from the envelope of the bulk dispersion, which has the form $\omega^2_{\rm bulk} = (q_y^2 - \beta q^2) + O(q^4)$ [1, 2] at small q. Thus equating $\omega_{\rm opt}$ to $\omega_{\rm band}$ yields $q_0 \propto v^{1/4}$ in agreement with our numerical calculations.

The finite v frequency dispersions of surface states in both the $X_{\rm nt}$ and $X_{\rm t}$ lattices (both with p1 symmetry) depicted in Fig. 2 are in general different on the top and bottom surfaces, as one would expect because opposite surfaces in lattices with such low symmetry are not equivalent. However, consistent with elastic theory, the small q Rayleigh waves on both surfaces are the same and do not reflect p1 symmetry. All of the higher frequency modes do however. The high-q frequencies of the acoustic modes of both lattices are different on the two surfaces as are all the higher-frequency optical surface modes [see SI].

The approach of the finite-frequency phonons to the topological phonons is also reflected in their inverse penetration depths κ shown in Figs. 2 (e) and (f). For both $X_{\rm nt}$ and $X_{\rm t}$, κ is the same for $v > 0$ at sufficiently small q on the bottom and top surfaces as predicted by elastic theory, but differences between the bottom and top surfaces arise as q becomes larger. As observed in the dispersion curves, the $v \to 0$ limit unfolds differently in the two lattices. For $X_{\rm nt}$, the $\mathrm{Re}(\kappa(q))$ curves of the two surfaces approach one another as v vanishes and eventually become identical across the entire SBZ. For $X_{\rm t}$, the $\mathrm{Re}(\kappa(q))$ curves of the top surface terminate at values of q that decrease with v whereas the $\mathrm{Re}(\kappa(q))$ curves of the acoustic and the lowest optical mode on the bottom surface approach each other to produce a two-fold degenerate zero-frequency mode at $v = 0$. Note that the penetration depth of the most dominant contribution to this mode diverges for $q \to 0$. The inset to Fig. 2 emphasizes the extremely small (but which we have verified is nonetheless positive) value of $\mathrm{Re}(\kappa(q))$ throughout the region that the surface acoustic mode exists on the top surface indicating a very large penetration depth.

Our results for the GKL with bending forces are very similar [see SI]. The only notable difference is that the interaction strength v is effectively larger than in the NNN model due to factors mandated by the rotational invariance of the bending energies. Apart from that, the approach of the finite-frequency phonons to the topological phonons is qualitatively the same.

We now outline how these results were obtained. The GKLs are derived from the standard kagome lattice (KL) by displacing [1] the 3 KL unit cell sites $\mathbf{r}_1 = (0, 0)$, $\mathbf{r}_2 = (1/2, 0)$, and $\mathbf{r}_3 = (1/4, \sqrt{3}/4)$ by

$$\delta\mathbf{r}_1(X) = \chi_1\sqrt{3}\,\mathbf{e}_1 - \chi_2\mathbf{a}_3\,, \tag{1a}$$

$$\delta\mathbf{r}_2(X) = \chi_2\sqrt{3}\,\mathbf{e}_2 - \chi_3\mathbf{a}_1\,, \tag{1b}$$

$$\delta\mathbf{r}_3(X) = \chi_3\sqrt{3}\,\mathbf{e}_3 - \chi_1\mathbf{a}_2\,, \tag{1c}$$

where $X \equiv (\chi_1, \chi_2, \chi_3)$ [28]. $\mathbf{a}_b$ are the normalized NN bond vectors of the KL: $\mathbf{a}_1 = (1, 0)$, $\mathbf{a}_2 = 1/2\,(-1, \sqrt{3})$, $\mathbf{a}_3 = 1/2\,(-1, -\sqrt{3})$. $\mathbf{e}_b$ are unit vectors perpendicular to the $\mathbf{a}_b$: $\mathbf{e}_1 = (0, -1)$, $\mathbf{e}_2 = 1/2\,(\sqrt{3}, 1)$, $\mathbf{e}_3 = 1/2\,(-\sqrt{3}, 1)$. The displacements are designed [1, 2] so that making one of the χ_b's nonzero causes filaments (i.e., sample traversing straight lines of bonds) parallel to $\mathbf{a}_b$ to zigzag while keeping the remaining filaments straight. The crystallographic symmetry of the resulting GKL depends on X. For example, the twisted KL with $X = (\chi, \chi, \chi)$ (where χ is some reasonable positive or negative number) has p31m symmetry [see SI]. For

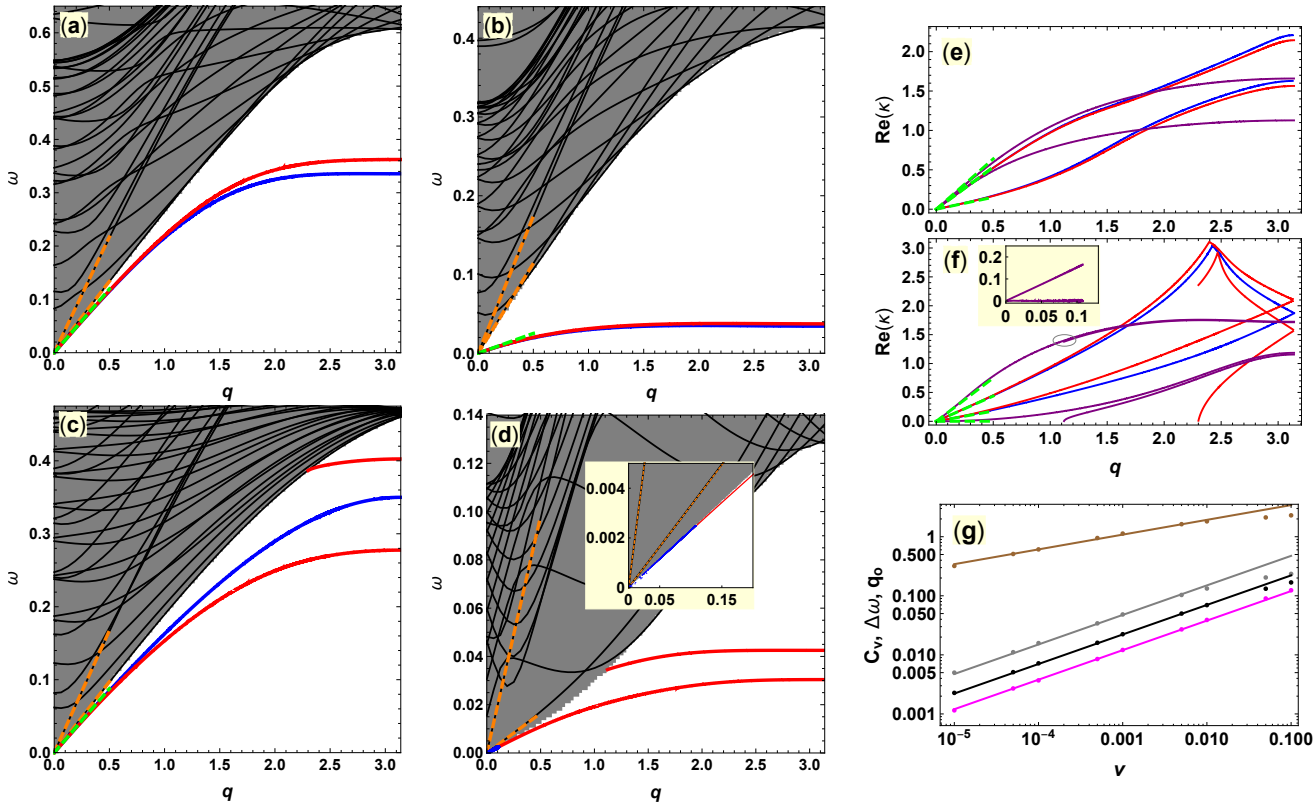

FIG. 2. Low-frequency mode structure for (a) $X_{\rm nt}$, $v = 0.1$; (b) $X_{\rm nt}$, $v = 0.001$; (c) $X_{\rm t}$, $v = 0.1$; (d) $X_{\rm t}$, $v = 0.001$. The gray areas are the projected bulk bands, and the black curves within these bands are bulk mode frequencies as a function of $q = q_x$ for different values of q_y, $q_y = 0, \pi/10, \pi/5, \ldots$. Note the strongly non-monotonic behavior of these modes for $X_{\rm t}$ at $v = 0.001$, a consequence of the lobes in density plots of the lowest mode at $v = 0$ with $\omega \sim (q_y^2 - \beta q_x^2)$ with $\beta > 0$ determined by $X_{\rm t}$ [1, 2]. The color codes for curves in (a)-(d) are red - bottom surface, blue - top surface, orange - longitudinal and transverse bulk sound modes at $q_y = 0$, and green - Rayleigh waves predicted by elasticity theory. Each surface mode is a linear combination of four modes that decay with y. The two smallest κ (largest penetration depths) are plotted in (e) [(f)] for each surface mode shown in (a) and (b) [(c) and (d)]. The color codes for these curves are red (blue) for bottom (top) surface modes at $v = 0.1$, purple for bottom and top acoustic modes and for the optical mode at $v = 0.001$, and dashed green for elastic theory results. Each of the purple curves in (e) consists of a nearly degenerate pair. The gray ellipsis in (f) highlights a hard-to-see onset of the acoustic mode after which the upper purple curve consists of a nearly degenerate pair. (g) c_R (gray) for $X_{\rm nt}$ and c_R (black), $\Delta\omega$ (magenta), and q_0 (brown) for $X_{\rm t}$. The lines in the corresponding colors are power-law fits with $c_R \sim \Delta\omega \sim v^{0.5}$ and $q_0 \sim v^{0.25}$, in agreement with our crude estimates. Note that the surface modes for $v = 0.001$ remain small and nearly flat throughout the SBZ implying low-energy point-like surface invaginations such as observed in Ref. [24].

$X = (0, \chi, \chi)$ and $X = (-\chi, \chi, \chi)$, the symmetry is reduced to cm and pm, respectively. Our generic GKLs have deformation parameters $X = X_{\rm nt} = (0.1, 0.15, 0.2)$ and $X = X_{\rm t} = (0.1, 0.15, -0.2)$. We have chosen these parameters so that the resulting GKLs have the lowest possible (p1) symmetry, and moderate distortions relative to the KL. Otherwise, these choices are arbitrary, and manifolds of alternative choices lead to qualitatively the same results.

The vibrational modes of an elastic network are governed by its dynamical matrix $\mathbf{D}$. In the bulk GKL, the equation of motion is simply $\omega^2\,\mathbf{u}(\mathbf{q}) = \mathbf{D}(\mathbf{q})\,\mathbf{u}(\mathbf{q})$, where $\mathbf{u} = (u_{1x}, u_{1y}, u_{2x}, u_{2y}, u_{3x}, u_{3y})$ is the displacement vector of the basis sites, $\mathbf{q}$ is the wave vector, and ω is the angular frequency. $\mathbf{D} = \mathbf{QSC}$ is the 6×6 lattice dynamical matrix (for unit mass at sites), with $\mathbf{Q}$ the equilibrium matrix, $\mathbf{C} = \mathbf{Q}^\dagger$ the compatibility matrix, and $\mathbf{S} = \mathrm{Diag}(1, 1, 1, v, v, v)$ the spring constant matrix (see Ref. [2] for background information). In the elastic (continuum) limit, $\mathbf{u}$ turns into a 2-component displacement field and $\mathbf{D}$ turns into a 2×2 effective dynamical matrix. Details about the dynamical matrices in the two theories are given in the SI.

To get a comprehensive picture, we use both lattice and elastic theory. In our elastic theory, we adapt the standard textbook calculation [27] of the decay lengths and sound velocities of acoustic surface phonons in isotropic continua to our anisotropic GLKs [see SI]. This approach applies only to the longest wavelength acoustic phonons. Our lattice-based calculations are a generalization to discrete lattices of the standard Rayleigh-wave continuum calculations [27]. Like the latter calculations, they are

done on semi-infinite systems that clearly separate top and bottom surfaces, yet they allow access to wave vectors ranging across the entire SBZ. To carry out our calculations, we break the lattice into one-cell-thick layers L, with $L = 0$ the surface layer, $L = 1$ the next layer into the bulk, and so on, stacked in the y-direction and with periodic boundary conditions along x. The equilibrium matrix has non-vanishing components $\mathbf{Q}_{L,L} \equiv \mathbf{Q}_{00}$ and $\mathbf{Q}_{L,L-1} \equiv \mathbf{Q}_{10}$ connecting sites in layer L to bonds in layers L and $L-1$, respectively; and the compatibility matrix has non-vanishing components $\mathbf{C}_{LL} \equiv \mathbf{C}_{00}$ and $\mathbf{C}_{L,L+1} \equiv \mathbf{C}_{01}$ connecting bonds in layer L to sites in layers L and $L+1$, respectively. The dynamical matrix then has components $\mathbf{D}_{L,L-1} = \mathbf{D}_{10} = \mathbf{Q}_{10}\mathbf{S}\mathbf{C}_{00}$, $\mathbf{D}_{LL} = D_{00} = \mathbf{Q}_{00}\mathbf{S}\mathbf{C}_{00} + \mathbf{Q}_{10}\mathbf{S}\mathbf{C}_{01}$, and $\mathbf{D}_{L,L+1} = \mathbf{Q}_{00}\mathbf{S}\mathbf{C}_{01}$. The equation of motion for any layer $L > 0$ then reads

$$\omega^2\,\mathbf{u}^L = \mathbf{D}_{10}\mathbf{u}^{L-1} + \mathbf{D}_{00}\mathbf{u}^L + \mathbf{D}_{01}\mathbf{u}^{L+1}\,, \qquad (2)$$

which is solved by $\mathbf{u}^{L+1} = Z\,\mathbf{u}^L$ provided that

$$\mathrm{Det}\big[\mathbf{D}_{10}Z^{-1} + \mathbf{D}_{00} + \mathbf{D}_{01}Z - \omega^2\,\boldsymbol{\delta}\big] = 0\,, \qquad (3)$$

where $\boldsymbol{\delta}$ is the unit matrix, and Z determines the the inverse decay length κ in the y-direction via $Z = \exp(-\kappa)$ (with κ in general complex). Solutions $Z(v,\omega,q)$ of Eq. (3) come in pairs with reciprocal magnitude. Solutions with $|Z(v,\omega,q)| = 1$ correspond to bulk modes, whereas solutions with $|Z(v,\omega,q)| < 1 (> 1)$ decay away from the bottom (top) surface and correspond to surface modes. The points in ω-q-space where bulk modes exist, i.e., points for which there is at least one pair of solutions with magnitude 1, form bands akin to the projected band structures in electronic systems (see Fig. 2). Surface modes can exist only within the bulk band gaps as the solutions of the equations of motion must obey the conditions imposed by the surface. Sites 1 and 2 of the surface unit cell lie directly in the free surface (note that site 3 does not). The force on these surface sites comes only from NN and NNN bonds 1 to 4 [Fig. 1] in the zeroth layer, and as a result for the free boundary condition we impose, the first four components of the force vector satisfy $\mathbf{f}^0 = \mathbf{D}_{00}\mathbf{u}^0 + \mathbf{D}_{01}\mathbf{u}^1 = \omega^2\mathbf{u}^0$. For $v > 0$, there are a total of eight zeros at any point in ω-q-space. This implies that, at any point in a band gap, there are four modes with $|Z(v,\omega,q)| < 1 (> 1)$ that decay away from the bottom (top) surface. The boundary conditions can be satisfied by superimposing these decaying modes,

$$\mathbf{u}^L = \sum_{n=1}^{4} A_n \mathbf{w}_n Z_n^L e^{iqx - i\omega t}\,, \qquad (4)$$

where the A_n are mode amplitudes and $\mathbf{w}_n = \mathbf{w}_n(v,\omega,q,Z_n)$ are polarization vectors. The band gap points for which the determinant of the 4×4 boundary matrix $\mathbf{B}$, defined by

$$B_{mn} = \sum_{k=1}^{6} \big[\mathbf{D}_{00} + \mathbf{D}_{01}Z_n - \omega^2\boldsymbol{\delta}\big]_{mk}\, w_{n,k}\,, \qquad (5)$$

vanishes determine the dispersion relation of the surface modes. To find these points, we use the standard secant-method for computing zeros with an array of starting points that sweeps the band gaps.

Modern $3d$ printing and cutting techniques now produce bespoke materials, including regular lattices, with almost arbitrary designs. In particular, these techniques can produce mechanical lattices, whose geometry is almost identical to isostatic mechanical NN topological lattices. To fully understand and control these lattices, it is important to know how their properties - elastic energy, bulk- and surface- mode structure, etc. - differ from those of the ideal NN isostatic lattice. Our formalism treats semi-infinite systems exactly and can easily be used to calculate linearized response, for example to a localized force at a surface.

The main result of the present work is the unravelling of the apparent dilemma of topological lattices where topological-phonon theory predicts for the example we are studying two soft surface modes on one surface (soft, bottom) and zero on the other (hard, top) whereas elasticity theory mandates that there be one Rayleigh wave per surface wavenumber on each surface and that the two waves have equal speeds. Our work shows that the resolution of the dilemma is as follows: as $v \to 0$, the domain of existence of the Rayleigh wave on the top surface shrinks to zero. On the bottom surface, there is a low-energy optical surface mode, whose domain grows to the full SBZ and which approaches the bottom surface Rayleigh wave as $v \to 0$. These two together produce the two surface-zero modes predicted by topological-phonon theory.

Our results provide guidance for interpreting results of experiments on metamaterials targeting topological phonons. Reference [25] reports experiments and finite element analysis on kagome-like lattices that show an asymmetric bulk phonon spectrum in a topological lattice but a symmetric one in a non-topological lattice. They verify the existence, in the same geometry we study, of the two low-energy surface modes on the soft surface that emerge from the two zero modes of the ideal topological lattice which they interpret as "an interesting departure from the conventional case of Rayleigh waves". Curiously neither the finite element analysis nor the measurements show any evidence of the acoustic Rayleigh wave on the hard surface mandated by elasticity theory. It would be interesting to see additional experiments that specifically target the evolution of the hard surface Rayleigh wave with increasing bending rigidity.

This work was supported by the NSF under No. DMR-1104701 (OS, TCL), No. DMR-1120901 (OS, TCL). TCL

was supported by a Simons Fellows grant.

[1] C. L. Kane and T. C. Lubensky, Nat. Phys. **10**, 39 (2014).
[2] T. C. Lubensky, C. Kane, X. Mao, A. Souslov, and K. Sun, Rep. Prog. Phys. **78**, 073901 (2015).
[3] X. M. Mao and T. C. Lubensky, "Maxwell lattices and topological mechanics," in *Annu. Rev. Condens. Matter Phys., Vol 9*, edited by S. Sachdev and M. C. Marchetti (2018) pp. 413–433.
[4] B. I. Halperin, Phys. Rev. B **25**, 2185 (1982).
[5] F. D. M. Haldane, Phys. Rev. Lett. **51**, 605 (1983).
[6] C. L. Kane and E. J. Mele, Phys. Rev. Lett. **95**, 226801 (2005).
[7] C. L. Kane and E. J. Mele, Phys. Rev. Lett. **95**, 146802 (2005).
[8] B. A. Bernevig, T. L. Hughes, and S. C. Zhang, Science **314**, 1757 (2006).
[9] J. E. Moore and L. Balents, Phys. Rev. B **75**, 121306 (2007).
[10] L. Fu, C. L. Kane, and E. J. Mele, Phys. Rev. Lett. **98**, 106803 (2007).
[11] M. Z. Hasan and C. L. Kane, Rev. Mod. Phys. **82**, 3045 (2010).
[12] X.-L. Qi and S.-C. Zhang, Rev. Mod. Phys. **83**, 1057 (2011).
[13] O. Stenull and T. C. Lubensky, Phys. Rev. Lett. **113**, 158301 (2014).
[14] J. Paulose, B. G.-g. Chen, and V. Vitelli, Nat. Phys. **11**, 153 (2015).
[15] J. Paulose, A. S. Meeussen, and V. Vitelli, PNAS **112**, 7639 (2015).
[16] D. Sussman, O. Stenull, and T. Lubensky, Soft Matter **12**, 6079 (2016).
[17] D. Z. Rocklin, B. G. G. Chen, M. Falk, V. Vitelli, and T. C. Lubensky, Phys. Rev. Lett. **116**, 135503 (2016).
[18] O. Stenull, C. L. Kane, and T. C. Lubensky, Phys. Rev. Lett. **117**, 068001 (2016).
[19] B. G. G. Chen, B. Liu, A. A. Evans, J. Paulose, I. Cohen, V. Vitelli, and C. D. Santangelo, Phys. Rev. Lett. **116**, 135501 (2016).
[20] A. S. Meeussen, J. Paulose, and V. Vitelli, Phys. Rev. X **6**, 041029 (2016).
[21] G. Baardink, A. Souslov, J. Paulose, and V. Vitelli, PNAS **115**, 489 (2018).
[22] D. Zhou, L. Y. Zhang, and X. M. Mao, Phys. Rev. Lett. **120**, 068003 (2018).
[23] D. Zhou, L. Zhang, and X. Mao, Topological Mechanics in Quasicrystals (2018).
[24] O. R. Bilal, R. Susstrunk, C. Daraio, and S. D. Huber, Advanced Materials **29**, 1700540 (2017).
[25] J. Ma, D. Zhou, K. Sun, X. Mao, and S. Gonella, Phys. Rev. Lett. **121**, 094301 (2018).
[26] X. Mao and T. C. Lubensky, Phys. Rev. E **83**, 011111 (2011).
[27] L. Landau and E. Lifshitz, *Theory of Elasticity, 3rd Edition* (Pergamon Press, New York, 1986).
[28] Our convention is equivalent to that of Ref. [1,2] with a change in the signs of the χ's, so that the topological polarization is $\mathbf{R}_T = -\frac{1}{2}\sum_\mu \mathbf{T}_\mu \,\mathrm{sign}\chi_\mu$, where $\mathbf{T}_\mu$ are the primitive translation vectors.